

HD 222237 b: a long-period super-Jupiter around a nearby star revealed by radial-velocity and *Hipparcos*–*Gaia* astrometry

Guang-Yao Xiao^{1b},^{1,2} Fabo Feng^{1b},^{1,2} Stephen A. Shectman,³ C. G. Tinney,⁴ Johanna K. Teske,⁵ B. D. Carter,⁶ H. R. A. Jones,⁷ Robert A. Wittenmyer,⁶ Matías R. Díaz,⁸ Jeffrey D. Crane,³ Sharon X. Wang,⁹ J. Bailey^{1b},⁴ S. J. O’Toole^{1b},¹⁰ Adina D. Feinstein,^{11†} Malena Rice,¹² Zahra Essack^{1b},¹³ Benjamin T. Montet,^{14,15} Avi Shporer¹⁶ and R. Paul Butler^{5★}

¹Tsung-Dao Lee Institute, Shanghai Jiao Tong University, 1 Lisuo Road, Shanghai 201210, P. R. China

²School of Physics and Astronomy, Shanghai Jiao Tong University, 800 Dongchuan Road, Shanghai 200240, P. R. China

³Observatories of the Carnegie Institution for Science, 813 Santa Barbara Street, Pasadena, CA 91101, USA

⁴School of Physics and Australian Centre for Astrobiology, University of New South Wales, Sydney, NSW 2052, Australia

⁵Earth and Planets Laboratory, Carnegie Institution for Science, 5241 Broad Branch Road, NW, Washington, DC 20015, USA

⁶Centre for Astrophysics, University of Southern Queensland, USQ Toowoomba, QLD 4350, Australia

⁷Centre for Astrophysics Research, University of Hertfordshire, College Lane, Hatfield (Herts) AL10 9AB, UK

⁸Las Campanas Observatory, Carnegie Institution of Washington, Colina El Pino, Casilla 601 La Serena, Chile

⁹Department of Astronomy, Tsinghua University, Beijing 100084, P. R. China

¹⁰Australian Astronomical Optics, Macquarie University, North Ryde, NSW 1670, Australia

¹¹Laboratory for Atmospheric and Space Physics, University of Colorado Boulder, UCB 600, Boulder, CO 80309, USA

¹²Department of Astronomy, Yale University, New Haven, CT 06511, USA

¹³Department of Physics and Astronomy, University of New Mexico, 210 Yale Blvd NE, Albuquerque, NM 87106, USA

¹⁴School of Physics, University of New South Wales, Sydney, NSW 2052, Australia

¹⁵UNSW Data Science Hub, University of New South Wales, Sydney, NSW 2052, Australia

¹⁶Department of Physics and Kavli Institute for Astrophysics and Space Research, Massachusetts Institute of Technology, Cambridge, MA 02139, USA

Accepted 2024 September 10. Received 2024 August 26; in original form 2023 October 27

ABSTRACT

Giant planets on long-period orbits around the nearest stars are among the easiest to directly image. Unfortunately these planets are difficult to fully constrain by indirect methods, e.g. transit and radial velocity (RV). In this study, we present the discovery of a super-Jupiter, HD 222237 b, orbiting a star located 11.445 ± 0.002 pc away. By combining RV data, *Hipparcos*, and multi-epoch *Gaia* astrometry, we estimate the planetary mass to be $5.19^{+0.58}_{-0.58} M_{\text{Jup}}$, with an eccentricity of $0.56^{+0.03}_{-0.03}$ and a period of $40.8^{+5.8}_{-4.5}$ yr, making HD 222237 b a promising target for imaging using the Mid-Infrared Instrument (MIRI) of *JWST*. A comparative analysis suggests that our method can break the inclination degeneracy and thus differentiate between prograde and retrograde orbits of a companion. We further find that the inferred contrast ratio between the planet and the host star in the *F1550C* filter ($15.50 \mu\text{m}$) is approximately 1.9×10^{-4} , which is comparable with the measured limit of the MIRI coronagraphs. The relatively low metallicity of the host star (-0.32 dex) combined with the unique orbital architecture of this system presents an excellent opportunity to probe the planet–metallicity correlation and the formation scenarios of giant planets.

Key words: techniques: radial velocities – astrometry – planetary systems – stars: individual: HD 222237.

1 INTRODUCTION

To date more than 5500 exoplanets have been discovered and confirmed via radial velocity (RV), transit, direct imaging, astrometry, and microlensing (Akeson et al. 2013). Among them, cold massive Jupiters play a crucial role in shaping the architecture and potential habitability of planetary systems, sparking significant interest in understanding their formation, evolution, and dynamics (e.g. Stevenson & Lunine 1988; Tsiganis et al. 2005). However, finding planets on

long-period orbits by precision velocity monitoring is painstaking. At least half an orbital period, preferably more, needs to be observed. For planets with periods of many decades, this can take an entire professional career or longer. Sufficiently precise velocities solve for all the orbital elements except inclination, so only the minimum mass of a planet ($m_p \sin i$) can be measured, where i is the unknown inclination angle.

To extend the temporal baseline and simultaneously solve for the inclination angle, a novel approach that combines RV data with astrometric data from both *Hipparcos* and *Gaia* data releases has been developed independently by several groups (e.g. Brandt 2018; Snellen & Brown 2018; Feng et al. 2019b; Kervella et al. 2019; Xuan & Wyatt 2020; Van Zandt & Petigura 2024). For instance,

★ E-mail: pbutler@carnegiescience.edu

† NHFP Sagan Fellow.

some researchers utilize archival RV data along with proper-motion anomalies between *Hipparcos* and *Gaia* astrometry to reveal the 3D stellar reflex motion perturbed by unseen companions and accurately determine the masses of long-period Jupiters (e.g. Li et al. 2021; Philipot et al. 2023; Xiao et al. 2023). However, it is important to note that the aforementioned methods generally use a single *Gaia* data release rather than multiple releases, which may result in unreliable constraints for planets with periods comparable to the time baseline of each satellite. Additionally, using proper-motion anomalies alone can introduce an inclination degeneracy, making it challenging to distinguish prograde ($0^\circ \leq i \leq 90^\circ$) and retrograde ($90^\circ < i \leq 180^\circ$) orbits of a planet (Kervella, Arenou & Schneider 2020). The prograde orbit aligns with the direction of increasing position angle (PA) on the sky, i.e. anticlockwise direction, while the retrograde orbit corresponds to a clockwise direction (see fig. 2.2 of Perryman 2018).

To overcome the above limitations, we have optimized our analysis to use multiple *Gaia* data releases by simulating the *Gaia* epoch data with Gaia Observation Forecast Tool¹ (GOST). We then employ a linear astrometric model to fit the synthetic data. By minimizing the difference between fitted and catalogue astrometry, we are able to uncover the non-linear reflex motion of a star. This approach has been successfully applied to refine the orbits of cold Jupiters around nearby stars (e.g. ϵ Ind A b and ϵ Eridani b, Feng et al. 2023). In this study, we present the discovery of a long-period super-Jupiter, orbiting a metal-poor nearby star HD 222237 on an eccentric orbit.

HD 222237 (= GJ 902, HIP 116745) is a K3 dwarf with a V magnitude of 7.09 (Gray et al. 2006; Koen et al. 2010), located at a heliocentric distance of 11.445 ± 0.002 pc (Gaia Collaboration 2021). It has an effective temperature of $T_{\text{eff}} = 4751 \pm 139$ K, a surface gravity of $\log g = 4.61 \pm 0.10$ dex, a metallicity of $[\text{Fe}/\text{H}] = -0.32 \pm 0.02$ dex, a mass of $M_\star = 0.76 \pm 0.09 M_\odot$, and a radius of $R_\star = 0.71 \pm 0.06 R_\odot$ (Stassun et al. 2019). The chromosphere of the star is slightly active with $\log R'_{\text{HK}} = -4.86$ (Tinney et al. 2002), and Ca II HK emission can be found in its spectra.

This paper is organized as follows. In Section 2, we describe the data and the adopted analysis method. The optimal orbital solution of HD 222237 b is presented in Section 3. The paper concludes with a brief discussion and summary in Section 4.

2 DATA AND METHODS

2.1 RV and astrometry data

The precision velocity monitoring of HD 222237 began in 1998 August with the UCLES echelle spectrometer on the 3.9 m Anglo-Australian Telescope (AAT; Diego et al. 1990). UCLES operated at moderate resolution, $R \sim 45\,000$. Wavelength calibration was provided by an Iodine cell (Marcy & Butler 1992). The data reduction, including the recovery of the spectrometer point spread function, is described in Butler et al. (1996). Due to its lower resolution (by modern standards), the precision of the AAT/UCLES system was limited to $\sim 3 \text{ m s}^{-1}$.

The High Accuracy Radial-velocity Planet Searcher (HARPS; Pepe et al. 2000) mounted on the ESO La Silla 3.6 m telescope began observing HD 222237 in 2003. The HARPS spectrograph underwent a major fibre link upgrade at the end of 2015 May (Lo Curto et al. 2015). We distinguish between the ‘HARPSpre’ and ‘HARPSpost’ data in Fig. 2. The RVs of HARPS spectra were reduced with the

SERVAL pipeline (Zechmeister et al. 2018) by Trifonov et al. (2020), and are publicly available at the HARPS-RVBANK archive.²

The Carnegie Planet Finder Spectrograph (PFS; Crane, Shectman & Butler 2006; Crane et al. 2008, 2010) mounted on the 6.5 m Magellan II telescope has been observing HD 222237 since 2011 August, extending the total RV baseline to about 25 yr. As with the AAT/UCLES system, PFS employs an Iodine cell for wavelength calibration to deliver high-precision RVs. The upper inflection point of the stellar reflex motion was observed by PFS in 2019, which enables a precise characterization of the orbital properties of the planet. The importance of spectrometer resolution to achieving precise RVs is illustrated by the difference in the quality of the UCLES data relative to HARPS and PFS, which operate at a resolution of 120 000–130 000. All the new RV data used in this work are presented in Table A1 and A2 of appendix.

To derive astrometric constraints, we use the *Hipparcos* epoch data [i.e. intermediate astrometry data (IAD)] from the new *Hipparcos* reduction of van Leeuwen (2007) and *Gaia* second and third data releases (GDR2 and GDR3; Gaia Collaboration 2018, 2023), as well as synthetic epoch data from GOST to perform joint analysis with RVs. The *Hipparcos* IAD and *Gaia* GOST data mainly comprise the scan angle ψ of the satellite, the along-scan (AL) parallax factor f^{AL} , and associated observation epoch at barycentre. Since the *Gaia* IAD are not available, we use GOST to predict the *Gaia* observations. The choice of *Hipparcos* version has negligible impact on our analyses, because we directly model the systematics in *Hipparcos* IAD using offsets and jitters for a given target (see Appendix B), and we are focusing on the temporal baseline between two satellites (~ 25 yr) when applying for long-period systems (Feng et al. 2023).

2.2 Methods

The complete methodology of jointly modelling RV and astrometry has been detailed in our previous work (Feng et al. 2019b, 2021, 2023); therefore, we provide a relatively brief introduction about the basic process. Further theoretical formulations can be found in Appendix B.

We first model the astrometry of the target system barycentre (TSB) at the GDR3 reference epoch. To solve the problem of perspective acceleration, we transform the above TSB astrometry from the equatorial coordinate system to the Cartesian system to obtain the state vector. The state vector is propagated to the *Hipparcos* epoch, and we then transform the new vector back to equatorial coordinate system (Lindgren et al. 2012; Feng et al. 2019a). Next, we simulate both GDR2 and GDR3 AL abscissae with GOST by adding the stellar reflex motion on to the linear motion of TSB, and fit a five-parameter model to the synthetic abscissae. That fitted astrometry, along with catalogue data, is used to construct the likelihood for GDR2 and GDR3. Likewise, we can also model the *Hipparcos* abscissae and calculate the corresponding likelihood. For the RV likelihood, we initially take into account all available noise proxies, e.g. *S*-index of PFS, bisector inverse span (Queloz et al. 2001) of HARPS and All Sky Automated Survey (Pojmanski 1997) photometry, and apply a moving average algorithm to model time-correlated noise in RVs (Feng, Tuomi & Jones 2017). However, we found this red noise model, compared with white noise model (e.g. jitter term for each instrument), has negligible impact on constraining the orbit in this work. Therefore, we choose the latter to construct the likelihood, which can significantly reduce the free parameters.

¹<https://gaia.esac.esa.int/gost/index.jsp>

²<https://cdsarc.u-strasbg.fr/viz-bin/cat/J/A+A/636/A74>

With the total likelihood ($\mathcal{L} = \mathcal{L}_{\text{RV}} \cdot \mathcal{L}_{\text{Hip}} \cdot \mathcal{L}_{\text{Gaia}}$), we finally derive the orbital solution by sampling the posterior via the parallel-tempering Markov Chain Monte Carlo (MCMC) sampler `ptemcee` (Vousden, Farr & Mandel 2016). `ptemcee` is extensively used for sampling from complex, high-dimensional, often multimodal probability distributions. It is capable of traversing different modes at higher temperatures, as well as exploring individual modes at lower temperatures, in order to avoid getting stuck in a local minimum. We employ 30 temperatures, 100 walkers, and 50 000 steps per chain to generate posterior distributions for all the fitting parameters, with the first 25 000 steps being discarded as burn-in. A Python script that incorporates our complete models (except for the red noise model) is available at <https://github.com/gyxiaotdli/mini-Agatha>.

The public package `orvara` (Brandt et al. 2021a) was also designed to fit full orbital parameters to any combination of RVs, relative and absolute astrometry. It uses the cross-calibrated absolute astrometry from an *Hipparcos–Gaia* catalogue of astrometric accelerations (HGCA; Brandt 2018), which corresponds to a single *Gaia* data release. However, our method with multiple data releases being incorporated is capable of enhancing the orbital constraint due to the inclusion of additional information. Besides, it is important to note that there is uncertainty in the estimation of the calibration parameters between *Hipparcos* and *Gaia* (Brandt 2018; Lindegren 2020). Considering this, our method adopts a case-by-case strategy that directly employs jitters and offsets to model astrometric systematics a posteriori. It has been proven effective to avoid the inflation of uncertainties during the frame transformation (Feng et al. 2021). Since our method is independent from aforementioned calibration, it can theoretically be applied to extensive *Gaia* sources whose *Hipparcos* measurements are not available, particularly for direct imaging systems without accessible RVs.

To justify the robustness of our detection, we initially conduct a comparative analysis between the widely used tool `orvara` (RV+HGCA) and our method without the incorporation of GDR2 (RV+HG3). Then we introduce GDR2 into our model (RV+HG23) and demonstrate the advantage of this inclusion in breaking the inclination degeneracy, thereby differentiating between prograde and retrograde orbits of the planet HD 222237 b.

3 RESULTS

As shown in Table 1, the primary fitted parameters of our method (both for RV+HG3 and RV+HG23) include the orbital period P , RV semi-amplitude K , eccentricity e , argument of periastron ω of stellar reflex motion, orbital inclination i , longitude of ascending node Ω , mean anomaly M_0 at the minimum epoch of RV data, and five astrometric offsets ($\Delta\alpha^*$, $\Delta\delta$, $\Delta\varpi$, $\Delta\mu_{\alpha^*}$, and $\Delta\mu_\delta$) of barycentre relative to GDR3. The semimajor axis a of the planet relative to the host, the mass of planet m_p , and the epoch of periastron passage T_p can be derived from above orbital elements. The priors for each parameter are listed in the last column. `orvara` also adopts `ptemcee` to fit nine parameters, including the primary star mass M_* , the secondary star mass m_p , a , $\sqrt{e} \sin \omega$, $\sqrt{e} \cos \omega$, i , Ω , mean longitude λ_{ref} at a reference epoch (2010.0 yr or JD = 2455197.50), and RV jitter (depends on the number of instruments). Some nuisance parameters, such as RV zero-point, parallax, and proper motion of system's barycentre, are marginalized by `orvara` to reduce computational costs. We use the same Gaussian priors for the stellar mass, while the default priors for the rest (i.e. log-uniform, uniform, geometric, see table 4 of Brandt et al. 2021a).

Combining RV and HGCA astrometry (EDR3 version, Brandt 2021), `orvara` yields a planetary mass of $4.66^{+0.63}_{-0.52} M_{\text{Jup}}$, a period of

$37.4^{+6.7}_{-3.8}$ yr, an eccentricity of $0.54^{+0.05}_{-0.03}$, and two possible inclinations of $56.5^{+5.3}_{-4.7}$ and $123.5^{+4.7}_{-5.3}$, respectively, corresponding to prograde and retrograde orbits. Other fitted and derived parameters are listed in Table 1, while the posterior distributions of selected parameters are displayed in Fig C1 of appendix. Fig. 1 shows the best-fitting Keplerian models to RVs and *Hipparcos–Gaia* astrometry, and the predicted location of HD 222237 b relative to its host star at epochs 2025.0. `orvara` predicts an angular separation (ρ) of 0.59 ± 0.05 arcsec and two possible PAs of $33 \pm 32^\circ$ and $182 \pm 16^\circ$ in 2025.0. It is evident that `orvara` cannot determine whether the planet is in retrograde or prograde orbital motion. Similar orbital solutions are also found by RV+HG3 (see Table 1), suggesting the reliability of our method and its consistency with `orvara`. Besides, its posterior distributions for i , Ω , $\Delta\alpha^*$, $\Delta\delta$, $\Delta\mu_{\alpha^*}$, and $\Delta\mu_\delta$ are clearly bimodal (Fig. C2) simply due to the fact that two data points (i.e. *Hipparcos* and GDR3 absolute astrometry) are insufficient to fully constrain the position and the proper motion of TSB if without a third data point (see the middle panel of Fig. 1).

To address the above limitations, it is crucial to incorporate GDR2 into our orbital fitting. The optimal orbit of HD 222237 b by RV+HG23 gives a slightly longer period of $40.8^{+5.8}_{-4.5}$ yr, an eccentricity of $0.56^{+0.03}_{-0.03}$, and a definite inclination of $49.9^{+3.4}_{-2.8}$, suggesting a prograde orbital motion. Given the stellar mass of $M_* = 0.76 \pm 0.09 M_\odot$, we derived a mass of $5.19^{+0.58}_{-0.58} M_{\text{Jup}}$ and a semimajor axis of $10.8^{+1.1}_{-1.0}$ au for the planet. The root mean squares of RV residuals for AAT, HARPSpre, HARPSpost, and PFS are, respectively 5.20 m s^{-1} , 1.72 m s^{-1} , 1.97 m s^{-1} , and 2.13 m s^{-1} , comparable with the instrument noise. We present the posterior distributions of selected orbital parameters in Fig. C3.

Figs 2 and 3 depict the optimal orbital solution for HD 222237 b based on the MCMC posterior of RV+HG23. The former shows the best fit to RVs, while the latter shows the best fit to *Hipparcos* IAD and *Gaia* GOST data, and the predicted position of the planet. In Fig. 3(a), we project the *Hipparcos* abscissae along the RA and Dec. directions for visualization purposes, and encode the observation time with colours. In Fig. 3(b), we use segments and shaded region to visualize the *Gaia* catalogue astrometry and the best-fitting astrometry. All of them have been corrected according to the TSB astrometry. The centre of the segment denotes the offset in RA and Dec. relative to the TSB, and the slope denotes the ratio of the proper motion offsets (PMo) in Dec. and RA, and the length is the product of PMo and the temporal baseline of GDR2 or GDR3. The fitted GDR2 and GDR3 shown in this panel are determined by fitting a five-parameter model to the synthetic data. Fig. 3(c) plots the 1D residual of *Hipparcos* abscissa between the observations and the best fit. In the last panel of Fig. 3, we predict the position of the planet on 2025 January 1. The estimated angular separation is 0.64 ± 0.04 arcsec, and the PA is $21 \pm 10^\circ$, consistent with the prediction based on `orvara` solution. This planet will reach its maximum angular separation of 1.45 ± 0.18 arcsec in 2040 January. In addition, we present a more intuitive comparison of our predictions with the five-parameter astrometry of GDR2 and GDR3 in Fig. 4. Overall, the fitting to GDR3 is better than GDR2 due to the longer temporal baseline.

As shown in Table 1, almost all the parameters (prograde orbital solution) from `orvara` and RV+HG3 are in great agreement within 1σ with the solution obtained by RV+HG23. With the inclusion of GDR2, our method can resolve the TSB ambiguity and is able to differentiate between prograde and retrograde orbits. To further corroborate this conclusion, we inject the posteriors of RV+HG3

Table 1. Parameters for HD 222237.

Parameter	Unit	Meaning	RV+HGCA ^d	RV+HG3	RV+HG23	Prior ^e
P	d	Orbital period	13648^{+2460}_{-1397}	13262^{+1319}_{-1165}	14892^{+2112}_{-1655}	$\text{Log}\mathcal{U}(-1, 16)$
K	m s^{-1}	RV semi-amplitude	$46.82^{+1.3}_{-0.95}$	$46.57^{+0.83}_{-0.82}$	$47.4^{+1.1}_{-1.0}$	$\mathcal{U}(10^{-6}, 10^6)$
e	–	Eccentricity	$0.54^{+0.05}_{-0.03}$	$0.53^{+0.03}_{-0.03}$	$0.56^{+0.03}_{-0.03}$	$\mathcal{U}(0, 1)$
ω	deg	Argument of periastris ^a	$3.1^{+1.4}_{-1.3}$	$3.2^{+1.4}_{-1.4}$	$2.6^{+1.3}_{-1.4}$	$\mathcal{U}(0, 2\pi)$
M_0	deg	Mean anomaly at JD 2451034	$269^{+14}_{-11} (20210)$	153^{+19}_{-20}	176^{+23}_{-23}	$\mathcal{U}(0, 2\pi)$
i	deg	Inclination	$56.5^{+5.3}_{-4.7} (123.5^{+4.7}_{-5.3})$	$57.8^{+4.9}_{-3.8} (122.9^{+3.3}_{-4.5})$	$49.9^{+3.4}_{-2.8}$	$\text{Cosi}\mathcal{U}(-1, 1)$
Ω	deg	Longitude of ascending node	$74.8^{+7.9}_{-8.5} (137.6^{+8.9}_{-8.3})$	$76.0^{+7.4}_{-6.1} (135.3^{+5.6}_{-6.9})$	$69.8^{+6.7}_{-5.7}$	$\mathcal{U}(0, 2\pi)$
$\Delta\alpha^*$	mas	α^* offset	–	$-0.45^{+0.26}_{-0.29} (-1.38^{+0.39}_{-0.36})$	$-0.79^{+0.34}_{-0.36}$	$\mathcal{U}(10^{-6}, 10^6)$
$\Delta\delta$	mas	δ offset	–	$1.87^{+0.33}_{-0.37} (-1.40^{+0.18}_{-0.14})$	$2.43^{+0.33}_{-0.36}$	$\mathcal{U}(10^{-6}, 10^6)$
$\Delta\mu_{\alpha^*}$	mas yr^{-1}	μ_{α^*} offset	$1.045^{+0.12}_{-0.080} (0.918^{+0.062}_{-0.048})$	$1.021^{+0.081}_{-0.083} (0.908^{+0.037}_{-0.044})$	$1.13^{+0.10}_{-0.10}$	$\mathcal{U}(10^{-6}, 10^6)$
$\Delta\mu_\delta$	mas yr^{-1}	μ_δ offset	$-0.044^{+0.087}_{-0.068} (-0.53^{+0.11}_{-0.14})$	$-0.050^{+0.063}_{-0.064} (-0.492^{+0.095}_{-0.083})$	$0.041^{+0.065}_{-0.068}$	$\mathcal{U}(10^{-6}, 10^6)$
$\Delta\varpi$	mas	ϖ offset	~ 0	$-0.005^{+0.018}_{-0.018}$	$-0.009^{+0.022}_{-0.022}$	$\mathcal{U}(10^{-6}, 10^6)$
P	yr	Orbital period	$37.4^{+6.7}_{-3.8}$	$36.3^{+3.6}_{-3.2}$	$40.8^{+5.8}_{-4.5}$	–
a	au	Semimajor axis ^b	$10.23^{+1.3}_{-0.83}$	$9.99^{+0.78}_{-0.71}$	$10.8^{+1.1}_{-1.0}$	–
m_p	M_{Jup}	Companion mass	$4.66^{+0.63}_{-0.52}$	$4.56^{+0.51}_{-0.49}$	$5.19^{+0.58}_{-0.58}$	–
$T_p - 2400\,000$	JD	Periastris epoch	45001^{+1403}_{-2472}	45387^{+1173}_{-1328}	43747^{+1661}_{-2116}	–
N^{AAT}	–	AAT observations ^c	35	35	35	–
N^{HARPSpre}	–	HARPSpre observations	43	43	43	–
$N^{\text{HARPSpost}}$	–	HARPSpost observations	10	10	10	–
N^{PFS}	–	PFS observations	63	63	63	–
γ^{AAT}	m s^{-1}	RV offset for AAT	$13.2^{+3.2}_{-1.9}$	$13.7^{+1.9}_{-1.9}$	$11.5^{+2.4}_{-2.8}$	$\mathcal{U}(10^{-6}, 10^6)$
γ^{HARPSpre}	m s^{-1}	RV offset for HARPSpre	$8.1^{+3.7}_{-2.5}$	$8.8^{+2.1}_{-2.2}$	$6.2^{+2.8}_{-3.0}$	$\mathcal{U}(10^{-6}, 10^6)$
$\gamma^{\text{HARPSpost}}$	m s^{-1}	RV offset for HARPSpost	$-22.2^{+3.7}_{-2.5}$	$-21.5^{+2.3}_{-2.3}$	$-24.1^{+2.9}_{-3.0}$	$\mathcal{U}(10^{-6}, 10^6)$
γ^{PFS}	m s^{-1}	RV offset for PFS	$-27.9^{+3.8}_{-2.6}$	$-27.2^{+2.2}_{-2.3}$	$-29.9^{+2.9}_{-3.0}$	$\mathcal{U}(10^{-6}, 10^6)$
J^{AAT}	m s^{-1}	RV jitter for AAT	$4.89^{+0.80}_{-0.67}$	$5.07^{+0.83}_{-0.73}$	$4.91^{+0.83}_{-0.69}$	$\mathcal{U}(0, 10^6)$
J^{HARPSpre}	m s^{-1}	RV jitter for HARPSpre	$1.68^{+0.23}_{-0.19}$	$1.70^{+0.23}_{-0.19}$	$1.72^{+0.23}_{-0.19}$	$\mathcal{U}(0, 10^6)$
$J^{\text{HARPSpost}}$	m s^{-1}	RV jitter for HARPSpost	$2.13^{+0.66}_{-0.44}$	$2.28^{+0.75}_{-0.50}$	$2.27^{+0.71}_{-0.48}$	$\mathcal{U}(0, 10^6)$
J^{PFS}	m s^{-1}	RV jitter for PFS	$1.99^{+0.24}_{-0.21}$	$2.03^{+0.25}_{-0.22}$	$2.02^{+0.25}_{-0.22}$	$\mathcal{U}(0, 10^6)$
J^{hip}	mas	Jitter for <i>Hipparcos</i>	–	$0.75^{+0.53}_{-0.48}$	$0.80^{+0.51}_{-0.50}$	$\mathcal{U}(0, 10^6)$
σ_{Gaia}	–	Error inflation factor	–	$1.00^{+0.10}_{-0.10}$	$1.59^{+0.07}_{-0.07}$	$\mathcal{N}(1, 0.1)$

Notes. ^aThe argument of periastron of the stellar reflex motion, differing by π with planetary orbit, i.e. $\omega_p = \omega + \pi$.

^bThe semimajor axis a and planet mass m_p are derived from fitted parameters assuming the stellar mass as a Gaussian prior.

^cThese four rows show the number of observations from each spectrometer.

^dThe orbital solution from *orvara*. Since some free parameters used by *orvara* differ from ours, we derive their values using MCMC posteriors.

^eThe priors of our method, while priors for *orvara* are listed in Brandt et al. (2021a). $\text{Log}\mathcal{U}(a, b)$ is the logarithmic uniform distribution between a and b , $\text{Cosi}\mathcal{U}(a, b)$ is the cosine uniform distribution between a and b , and $\mathcal{N}(a, b)$ is the Gaussian distribution with mean a and standard deviation b .

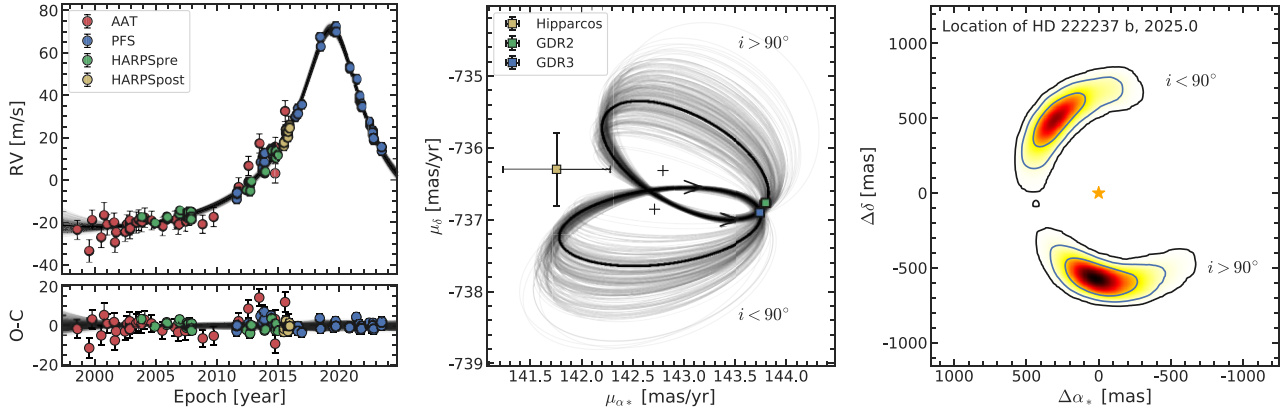


Figure 1. *orvara* fits to RV and *Hipparcos*–*Gaia* astrometry. Left panel: RV curve of HD 222237 b. The points with error bar denote the RV measurements and associated uncertainties. The thick black line shows the best-fitting orbit. Residuals (O-C) between the observation and the model are plotted below. Middle panel: astrometric acceleration in right ascension and declination. Two sets of orbits with equivalent likelihood are displayed. The thick lines indicate two best-fitting solutions separated by inclination, while the thin line indicate the possible orbital solutions randomly drawn from the MCMC chain. The plus symbols denote the proper motion of TSB, and the arrows indicate the direction in which the proper motion varies over time. The GDR2 astrometry (not used in *orvara* and RV+HG3 fittings) is added for subsequent analyses. It is evident that two astrometric data points (e.g. *Hipparcos* and GDR3) cannot distinguish two possible solutions, but the inclusion of GDR2 might be helpful to change this situation. Right panel: the predicted position of HD 222237 b on 2025 January 1 and associated 1σ , 2σ , 3σ uncertainties (contour lines). Two possible sets of contours correspond to prograde ($i < 90^\circ$) or retrograde ($i > 90^\circ$) orbits. The orange star denotes the host star HD 222237.

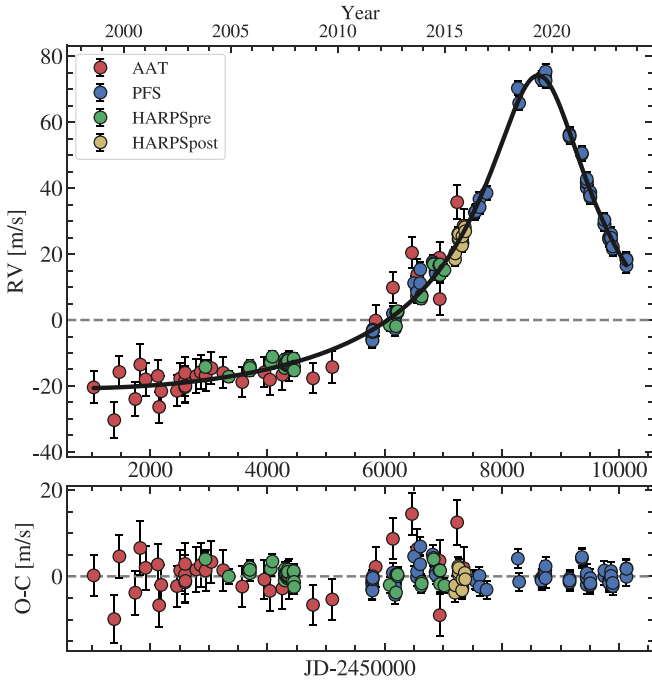


Figure 2. RV+HG23 fits to RVs. The symbols are the same as in the left panel of Fig. 1.

into RV+HG23 model and inspect whether the two sets of orbital solution from the former can be distinguished by the latter (Fig. C4). It can be found that the higher inclination (corresponding to the retrograde orbital solution) will be rejected by RV+HG23 model, suggesting the precision of *Gaia*, along with the baseline between GDR2 and GDR3, is sufficient to obtain an unambiguous orbital orientation of HD 222237 b. It should also be noted that the use of multiple *Gaia* DRs does not significantly improve the constraint on long-period orbits, but it can provide additional information about

the raw abscissae and thus improve the accuracy of the orbital solutions.

4 DISCUSSION AND SUMMARY

In this paper, we report the discovery of a long-period and eccentric super-Jupiter HD 222237 b located 11.445 ± 0.002 pc away from our Solar system, based on combined analyses of RV, *Hipparcos*, and multiple epochs of *Gaia* astrometry. The planet has $P = 40.8^{+5.8}_{-4.5}$ yr, $e = 0.56^{+0.03}_{-0.03}$, $i = 49.9^{+3.4}_{-2.8}$, and $m_p = 5.19^{+0.58}_{-0.58} M_{\text{Jup}}$. Compared with *orvara*, which only utilizes proper-motion anomalies data, our methodology with multiple *Gaia* data releases being incorporated can avoid the ambiguity of inclination. Consequently, we highlight the advantage of our approach for characterizing the orbital properties of cold Jupiters.

There are some possible caveats about our method. We note that there may be unknown biases associated with using both GDR2 and GDR3. But their solutions are relatively independent apart from the common data they share. On the other hand, correlated data can be used to detect signals if the correlation is well modelled, such as how we detect planets in RV data polluted by time-correlated noise. All the noise in GDR2 and GDR3 would not significantly influence our results if they are not significantly time-correlated. Unlike Feng et al. (2023) who uses all of the GOST predictions to model *Gaia* abscissae, we have excluded those that fall into the observation gaps (or satellite dead times³) in this work. To further validate the impact of these gaps, we conducted a test to compare the mass of HD 222237 b derived from solutions with and without correcting for the gaps. The difference in planet mass is found to be relatively small ($0.28 M_{\text{Jup}}$), which is within the 1σ uncertainty reported in this work. Regarding the assumption that all *Gaia* abscissae have the same uncertainty, we note that this is reasonable as long as the uncertainties are not significantly time-dependent. While this assumption may affect the precision of the orbital solution, it only becomes significant when

³<https://www.cosmos.esa.int/web/gaia/dr3-data-gaps>

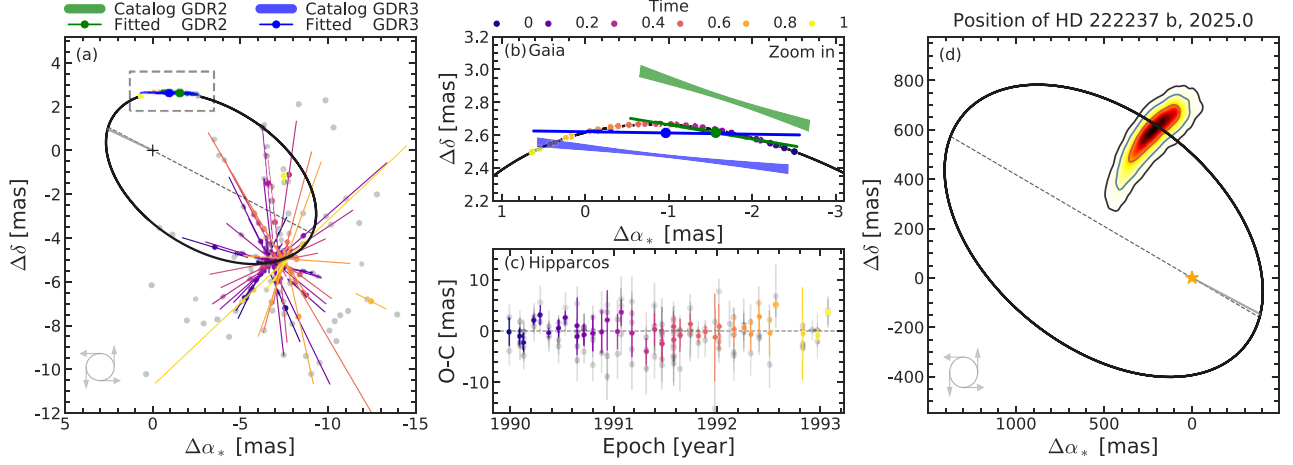


Figure 3. RV+HG23 fits to *Hipparcos* and *Gaia* astrometry. (a) The best-fitting astrometric orbit of HD 222237. The black dashed line inside the orbit is the line of nodes joining the ascending node and the descending node. The plus symbol denotes the system’s barycentre, and the grey line connects it with the periastron. The post-fit *Hipparcos* abscissa residuals are projected into the RA and Dec. axes (grey dots). Their multiple measurements of each epoch have been binned to single points with colours, and the brightness of colours gradually increases with observation time (the temporal baseline of each satellite is set to 1). The orientations of the error bars of each point denote the AL direction of *Hipparcos*. (b) Zoom in on the rectangle region of panel (a) depicts the best fit to *Gaia* GOST data and the comparison between the best-fitting and catalogue astrometry (positions and proper motions) at GDR2 and GDR3 reference epochs. The shaded regions represent the uncertainty of catalogue positions and proper motions after removing TSB motion. The dot and slope of two lines (blue and green) indicate the best-fitting position and PMo induced by the planet. (c) The residual (O-C) of *Hipparcos* abscissa. (d) The predicted position of HD 222237 b on 2025 January 1 and associated 1σ , 2σ , 3σ uncertainties (contour line). The curl at the lower left corner denotes the orientation of the orbital motion.

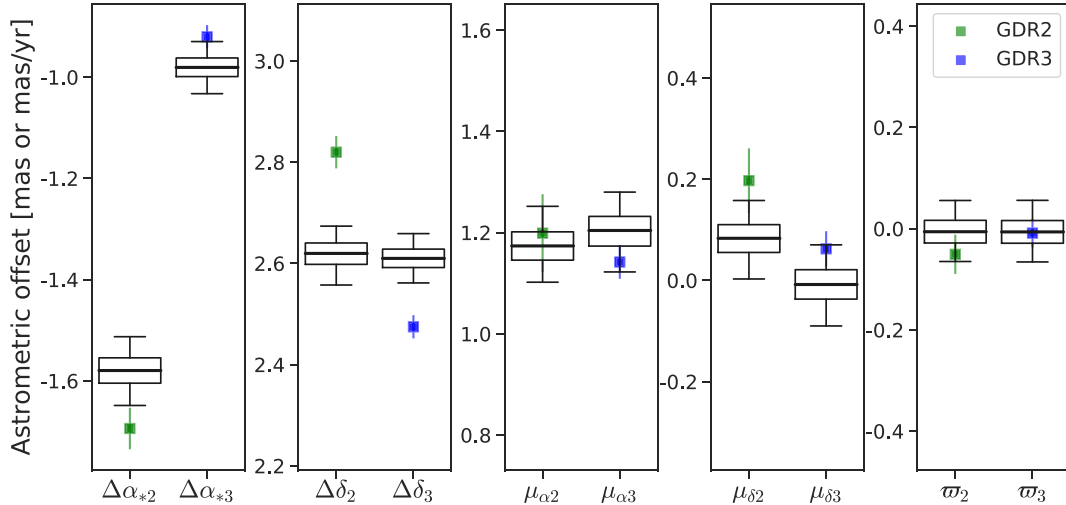


Figure 4. Comparing the five-parameter astrometry of the model prediction to GDR2 and GDR3 astrometry. The barycentric motion has been subtracted for both catalogue *Gaia* data (square) and the prediction (boxplot). The inner thick line, the body, and the edge of the boxplot, respectively, indicate the median, 1σ uncertainty, and 3σ uncertainty. The subscripts of the label of the x-axis correspond to the *Gaia* release number.

the required precision is well below ~ 1 per cent (see section 6.1.1 of Brandt et al. 2021b).

Fig. 5 shows the location of the planet in eccentricity–semimajor axis and mass–angular separation spaces. As can be seen in the left panel, HD 222237 b has a relatively eccentric orbit in comparison to any exoplanets discovered at large separations (> 10 au). Additionally, the large angular separation (right panel) places it among the small number of cold giant planets that are amenable to further direct imaging characterizations. For the next few years, the planet will continue to move away from its host (Fig. 3), presenting an excellent opportunity to perform such imaging. Using

the ATMO 2020 cooling tracks⁴ with the assumption of chemical equilibrium for the planetary atmosphere (Phillips et al. 2020), we estimate an effective temperature of 217 ± 6 K ($\lambda_{\max} \sim 13.3 \mu\text{m}$) for HD 222237 b by adopting an age of 7.54 ± 0.87 Gyr (Lovis et al. 2011) derived through the activity–rotation–age calibration (Mamajek & Hillenbrand 2008). We also estimate an upper limit of equilibrium temperature of 61 K using

$$T_{\text{eq}} = T_{\text{eff}\star}(1 - A_B)^{1/4} \sqrt{\frac{R_\star}{2a}}, \quad (1)$$

⁴<https://perso.ens-lyon.fr/isabelle.baraffe/ATMO2020/>

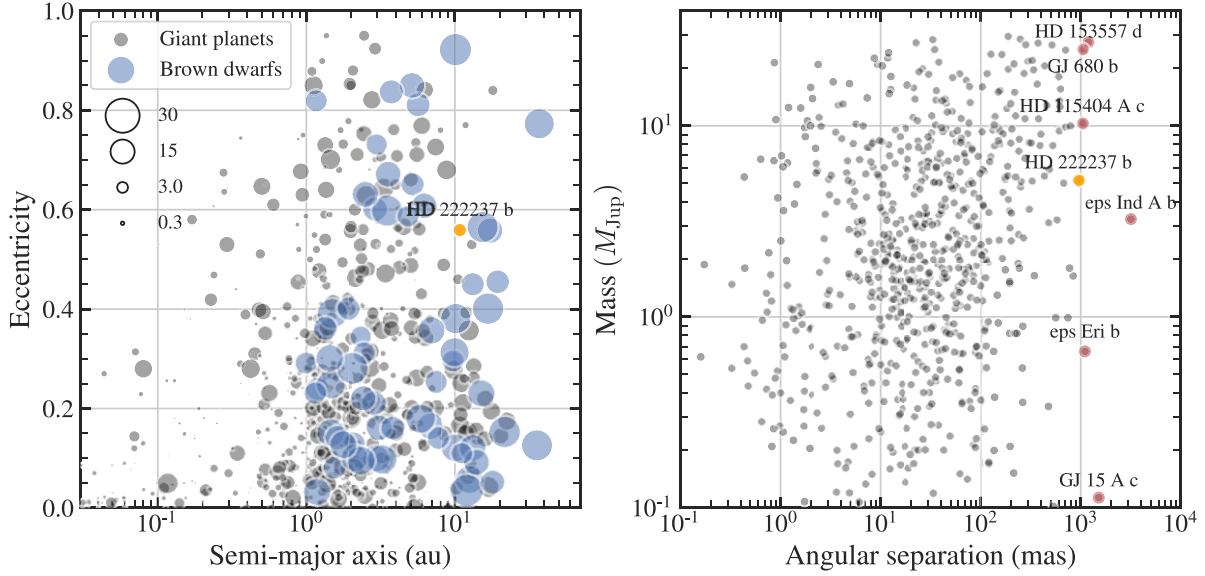


Figure 5. Left panel: eccentricity versus semimajor axis for RV-detected companions. The size of circles is proportional to the planetary (minimum) mass. Right panel: planetary (minimum) mass versus angular separation. HD 222237 b is marked by an orange circle. We also show six substellar companions with orbits at the widest separation. All the data points are compiled from the NASA exoplanet archive (Akeson et al. 2013) on 2024 July 1.

where A_B is the Bond albedo ($A_B = 0$), a is the semimajor axis of the planet, and $T_{\text{eff},\star}$ and R_\star are stellar effective temperature and radius, respectively. Then assuming a blackbody radiation for the host star HD 222237, we can calculate its apparent (Vega) magnitude in different bandpass according to the filter response,⁵ the Vega spectrum, and the distance. Although based on the planetary mass and the system age, the absolute magnitude of the planet can be directly obtained through the interpolation⁶ of the cooling tracks (ATMO 2020 models provide pre-calculated absolute magnitudes in a number of common photometric filters). These absolute magnitudes will be converted to apparent magnitudes assuming the planet has the same distance as the star. Ultimately, the contrast ratios of the planet to its host in different filters can be inferred.

We found that the contrast ratios in J , H , and K bands are as low as $\sim 10^{-10}$, significantly lower than the typical contrast limit ($\sim 10^{-6}$) of the current ground-based coronagraphs, such as SCExAO/CHARIS installed on the Subaru telescope (Jovanovic et al. 2015; Currie et al. 2020). This means the planet is undetectable in near-infrared band by those facilities, but it may be detectable using the Mid-Infrared Instrument (MIRI) (Rieke et al. 2015) mounted on *JWST*. Fig. 6 shows the derived contrast ratios of the system in different *JWST*/MIRI coronagraph filters. It is significant that the inner working angles (IWA) of three four-quadrant phase masks (Rouan et al. 2000) coronagraphs are smaller than the planet–star separation at epoch 2025.0. Furthermore, when comparing the actual performance (Boccaletti et al. 2022, see their fig. 5) of the MIRI coronagraphs, we found the *F1550C* filter with reference star subtraction and long integrations seems appropriate for imaging the planet, even if we adopt a more broader assumption of the system age.

In addition, we explore the contribution of planetary reflected light on the contrast. The flux ratio of the planet to the host star is expressed

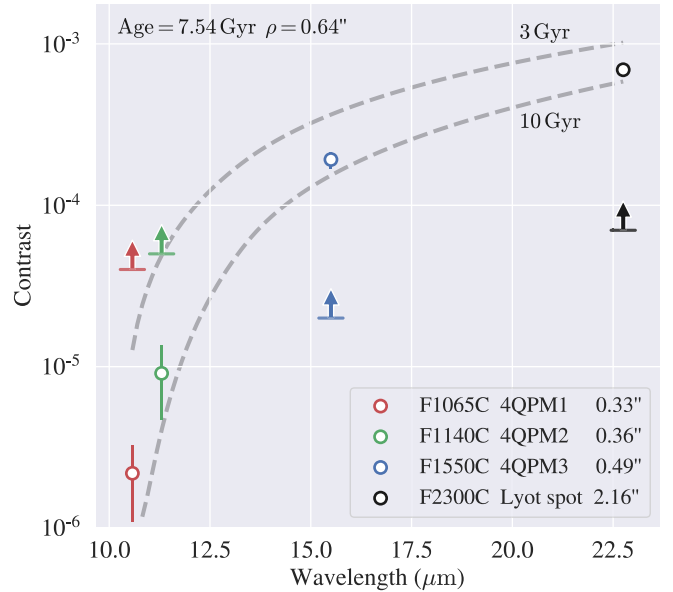


Figure 6. Contrast ratio with respect to MIRI coronagraphy filters. The legend shows the filter, coronagraph, and the IWA of MIRI, while the coloured circles with error bar represent the estimated contrast ratios assuming an age of 7.54 ± 0.87 Gyr. The ratios for *F1065C*, *F1140C*, *F1550C*, and *F2300C* are $2.2(1.1) \times 10^{-6}$, $9.1(4.4) \times 10^{-6}$, $1.9(0.2) \times 10^{-4}$, and $6.9(0.5) \times 10^{-4}$, respectively (the numbers in parentheses denote the associated errors). The upward-pointing arrows denote the measured contrast limits by Boccaletti et al. (2022). The grey dashed lines denote the conservative estimates of contrast ratios assuming a system age of 3 and 10 Gyr, respectively. *F1550C* has contrast ratio and IWA larger than the limit, even if the age of the system ranges from 3 to 10 Gyr.

as (e.g. Kane & Gelino 2010, equation 7)

$$\frac{f_p(\phi, \lambda)}{f_\star(\lambda)} = A_g(\lambda) g(\phi, \lambda) \frac{R_p^2}{r^2}, \quad (2)$$

⁵Download from the SVO Filter Profile Service: <http://svo2.cab.inta-csic.es/theory/fps3/>

⁶Using the python `scipy.interpolate.interp1d` library

where ϕ is the phase angle, $A_g(\lambda)$ is the geometric albedo ranging from 0 to 1, $g(\phi, \lambda)$ is the phase function ranging from 0 to 1, r is the distance to the star, and R_p is the planetary radius that can be obtained by interpolating the cooling tracks. Assuming $g = 1$ and $A_g = 0.5$, the magnitude of the contrast ratio is estimated to be $\sim 10^{-9}$, larger than those derived from cooling model in near-infrared band, but it remains undetectable. Nevertheless, this suggests that the thermal emission of the planet in the near-infrared band might be dominated by the reflection of starlight instead of self-luminosity.

Bowler, Blunt & Nielsen (2020) suggested that, based on their population-level eccentricity analysis examining directly imaged substellar companions, companions with $M_p < 15 M_{\text{Jup}}$ tend to have relatively lower orbital eccentricity, while brown dwarfs (BDs) exhibit higher eccentricity. The authors interpreted this as evidence for imaged planets formed through core accretion, and for BDs formed through molecular cloud fragmentation. We note, however, that HD 222237 b has an eccentricity of $0.56^{+0.03}_{-0.03}$, implying the possibility of experiencing some kinds of severe orbital evolution, such as planet–planet scattering (e.g. Ford & Rasio 2008) or perturbations from third-body fly-by (e.g. Naoz 2016). Furthermore, the metal-poor condition (-0.32 dex) along with the wide separation appears to contradict the predictions of the core accretion paradigm (e.g. Ida & Lin 2004; Mordasini et al. 2012), although we cannot rule out that the core of the planet initially formed on small separation and then underwent outward scattering and runaway accretion (Marleau et al. 2019). On the other hand, disc instability is thought to be metal-independent and occurs far away from the central star (> 10 au), where it allows for more efficient cooling and collapse, resulting in the formation of massive companions (e.g. Meru & Bate 2010; Rice 2022). Some works pointed out that giant planets might not prefer orbiting metal-rich hosts above a limit of $\sim 4 M_{\text{Jup}}$, i.e. more massive planets might show similar formation channel with BDs (e.g. Santos et al. 2017; Schlaufman 2018; Maldonado et al. 2019). The population synthesis model (Forgan et al. 2018) predicts that it is possible for some massive companions to undergo inward migration (Baruteau, Meru & Paardekooper 2011) and tidal disruption (Nayakshin 2017) to decrease their mass on a much closer-in and eccentric orbit (Rice 2022). In conclusion, it is likely that disc instability is responsible for the formation of HD 222237 b, but we cannot exclude a formation by core accretion at small separation. This system would benefit from high-contrast imaging studies to disentangle the truth from the ambiguities of its formation and dynamics.

ACKNOWLEDGEMENTS

We thank the anonymous referees for their insightful comments and valuable suggestions that greatly improved our paper. This research is supported by Shanghai Jiao Tong University 2030 Initiative. This research is also supported by the National Natural Science Foundation of China (NSFC) under grant no. 12473066, and the Chinese Academy of Sciences President's International Fellowship Initiative grant no. 2020VMA0033. MR acknowledges support from Heising–Simons Foundation grant #2023-4478. The authors acknowledge the years of technical support from LCO staff in the successful operation of PFS, enabling the collection of the data presented in this paper. We also thank Samuel W. Yee for his effort on the observations and Pablo Peña for his valuable cross-check of orbital period. This work is based in part on data acquired at the Anglo-Australian Telescope. We acknowledge the traditional custodians of the land on which the AAT stands, the Gamilaraay people, and pay our respects to elders past and present. The computations in this paper were run on the

π 2.0 (or the Siyuan-1) cluster supported by the Center for High Performance Computing at Shanghai Jiao Tong University.

This research has made use of the SIMBAD data base, operated at CDS, Strasbourg, France (Wenger et al. 2000). This work presents results from the European Space Agency (ESA) space mission *Gaia*. *Gaia* data are being processed by the *Gaia* Data Processing and Analysis Consortium (DPAC). Funding for the DPAC is provided by national institutions, in particular the institutions participating in the *Gaia* MultiLateral Agreement (MLA). The *Gaia* mission website is <https://www.cosmos.esa.int/gaia>. The *Gaia* archive website is <https://archives.esac.esa.int/gaia>. This paper is partly based on observations collected at the European Organisation for Astronomical Research in the Southern Hemisphere under ESO programmes: 192.C-0852, 072.C-0488, 183.C-0972. This research has made use of the SVO Filter Profile Service "Carlos Rodrigo", funded by MCIN/AEI/10.13039/501100011033/ through grant PID2020-112949GB-I00.

This paper includes data gathered with the 6.5 m Magellan Telescopes located at Las Campanas Observatory, Chile.

DATA AVAILABILITY

The PFS and AAT RV data are available in the appendix, while other data are publicly available.

REFERENCES

- Akeson R. L. et al., 2013, *PASP*, 125, 989
- Baruteau C., Meru F., Paardekooper S.-J., 2011, *MNRAS*, 416, 1971
- Boccaletti A. et al., 2022, *A&A*, 667, A165
- Bowler B. P., Blunt S. C., Nielsen E. L., 2020, *AJ*, 159, 63
- Brandt G. M. et al., 2021b, *AJ*, 162, 301
- Brandt T. D., 2018, *ApJS*, 239, 31
- Brandt T. D., 2021, *ApJS*, 254, 42
- Brandt T. D., Dupuy T. J., Li Y., Brandt G. M., Zeng Y., Michalik D., Bardalez Gagliuffi D. C., Raposo-Pulido V., 2021a, *AJ*, 162, 186
- Butler R. P., Marcy G. W., Williams E., McCarthy C., Dosanji P., Vogt S. S., 1996, *PASP*, 108, 500
- Crane J. D., Shectman S. A., Butler R. P., 2006, in McLean I. S., Iye M., eds, Proc. SPIE Conf. Ser. Vol. 6269, Ground-Based and Airborne Instrumentation for Astronomy. SPIE Bellingham, p. 626931
- Crane J. D., Shectman S. A., Butler R. P., Thompson I. B., Birk C., Jones P., Burley G. S., 2010, in McLean I. S., Ramsay S. K., Takami H., eds, Proc. SPIE Conf. Ser. Vol. 7735, Ground-Based and Airborne Instrumentation for Astronomy III. SPIE, Bellingham, p. 773553
- Crane J. D., Shectman S. A., Butler R. P., Thompson I. B., Burley G. S., 2008, in McLean I. S., Casali M. M., eds, Proc. SPIE Conf. Ser. Vol. 7014, Ground-Based and Airborne Instrumentation for Astronomy II. SPIE, Bellingham, p. 701479
- Currie T. et al., 2020, in Schreiber L., Schmidt D., Vernet E., eds, Proc. SPIE Conf. Ser. Vol. 11448, Adaptive Optics Systems VII. SPIE, Bellingham, p. 114487H
- Diego F., Charalambous A., Fish A. C., Walker D. D., 1990, in Crawford D. L., ed., Proc. SPIE Conf. Ser. Vol. 1235, Instrumentation in Astronomy VII. SPIE, Bellingham, p. 562
- Feng F. et al., 2021, *MNRAS*, 507, 2856
- Feng F., Anglada-Escudé G., Tuomi M., Jones H. R. A., Chanamé J., Butler R. P., Janson M., 2019b, *MNRAS*, 490, 5002
- Feng F., Butler R. P., Vogt S. S., Holden B., Rui Y., 2023, *MNRAS*, 525, 607
- Feng F., Lisogorskyi M., Jones H. R. A., Kopeikin S. M., Butler R. P., Anglada-Escudé G., Boss A. P., 2019a, *ApJS*, 244, 39
- Feng F., Rui Y., Xuan Y., Jones H., 2024, *ApJS*, 271, 50
- Feng F., Tuomi M., Jones H. R. A., 2017, *MNRAS*, 470, 4794
- Ford E. B., Rasio F. A., 2008, *ApJ*, 686, 621
- Forgan D. H., Hall C., Meru F., Rice W. K. M., 2018, *MNRAS*, 474, 5036

- Gaia Collaboration, 2018, *A&A*, 616, A1
- Gaia Collaboration et al., Brown A. G. A.), 2021, *AAP*, 649, A1
- Gaia Collaboration, 2023, *A&A*, 674, A1
- Gray R. O., Corbally C. J., Garrison R. F., McFadden M. T., Bubar E. J., McGahee C. E., O'Donoghue A. A., Knox E. R., 2006, *AJ*, 132, 161
- Halbwachs J.-L. et al., 2023, *A&A*, 674, A9
- Holl B. et al., 2023, *A&A*, 674, A10
- Ida S., Lin D. N. C., 2004, *ApJ*, 616, 567
- Jovanovic N. et al., 2015, *PASP*, 127, 890
- Kane S. R., Gelino D. M., 2010, *ApJ*, 724, 818
- Kervella P., Arenou F., Mignard F., Thévenin F., 2019, *A&A*, 623, A72
- Kervella P., Arenou F., Schneider J., 2020, *A&A*, 635, L14
- Koen C., Kilkeny D., van Wyk F., Marang F., 2010, *MNRAS*, 403, 1949
- Li Y. et al., 2021, *AJ*, 162, 266
- Lindgren L., 2020, *A&A*, 633, A1
- Lindgren L., Lammers U., Hobbs D., O'Mullane W., Bastian U., Hernández J., 2012, *A&A*, 538, A78
- Lo Curto G. et al., 2015, *The Messenger*, 162, 9
- Lovis C. et al., 2011, preprint ([arXiv:1107.5325](https://arxiv.org/abs/1107.5325))
- Maldonado J., Villaver E., Eiroa C., Micela G., 2019, *A&A*, 624, A94
- Mamajek E. E., Hillenbrand L. A., 2008, *ApJ*, 687, 1264
- Marcy G. W., Butler R. P., 1992, *PASP*, 104, 270
- Marleau G.-D., Coleman G. A. L., Leleu A., Mordasini C., 2019, *A&A*, 624, A20
- Meru F., Bate M. R., 2010, *MNRAS*, 406, 2279
- Mordasini C., Alibert Y., Benz W., Klahr H., Henning T., 2012, *A&A*, 541, A97
- Naoz S., 2016, *ARA&A*, 54, 441
- Nayakshin S., 2017, *Publ. Astron. Soc. Aust.*, 34, e002
- Pepe F. et al., 2000, in Iye M., Moorwood A. F., eds, *Proc. SPIE Conf. Ser. Vol. 4008, Optical and IR Telescope Instrumentation and Detectors*. SPIE, Bellingham, 582
- Perryman M., 2018, *The Exoplanet Handbook*, 2nd edn. Cambridge Univ. Press, Cambridge, p. 952
- Philipot F., Lagrange A. M., Rubini P., Kiefer F., Chomez A., 2023, *A&A*, 670, A65
- Phillips M. W. et al., 2020, *A&A*, 637, A38
- Pojmanski G., 1997, *Acta Astron.*, 47, 467
- Queloz D. et al., 2001, *A&A*, 379, 279
- Rice K., 2022, *Oxford Research Encyclopedia of Planetary Science*, Oxford University Press. p. 250
- Rieke G. H. et al., 2015, *PASP*, 127, 584
- Rouan D., Riaud P., Boccaletti A., Clénet Y., Labeyrie A., 2000, *PASP*, 112, 1479
- Santos N. C. et al., 2017, *A&A*, 603, A30
- Schlaufman K. C., 2018, *ApJ*, 853, 37
- Snellen I. A. G., Brown A. G. A., 2018, *Nat. Astron.*, 2, 883
- Stassun K. G. et al., 2019, *AJ*, 158, 138
- Stevenson D. J., Lunine J. I., 1988, *Icarus*, 75, 146
- Tinney C. G., McCarthy C., Jones H. R. A., Butler R. P., Carter B. D., Marcy G. W., Penny A. J., 2002, *MNRAS*, 332, 759
- Trifonov T., Tal-Or L., Zechmeister M., Kaminski A., Zucker S., Mazeh T., 2020, *A&A*, 636, A74
- Tsiganis K., Gomes R., Morbidelli A., Levison H. F., 2005, *Nature*, 435, 459
- van Leeuwen F., 2007, *A&A*, 474, 653
- Van Zandt J., Petigura E. A., 2024, *AJ*, 167, 250
- Vousden W. D., Farr W. M., Mandel I., 2016, *MNRAS*, 455, 1919
- Wenger M. et al., 2000, *A&AS*, 143, 9
- Xiao G.-Y. et al., 2023, *Res. Astron. Astrophys.*, 23, 055022
- Xuan J. W., Wyatt M. C., 2020, *MNRAS*, 497, 2096
- Zechmeister M. et al., 2018, *A&A*, 609, A12

APPENDIX A: RVS FOR HD 222237

Table A1. PFS RVs for HD 222237.

BJD	RV [m s^{-1}]	Error [m s^{-1}]	S-index	BJD	RV [m s^{-1}]	Error [m s^{-1}]	S-index
2455785.74573	−30.19	0.91	0.227	2458717.64622	47.90	0.79	0.212
2455787.83202	−30.82	0.96	0.186	2458738.67411	48.70	0.89	0.203
2455787.83472	−31.86	0.95	0.187	2458738.67807	47.74	0.92	0.201
2455790.76822	−32.10	1.04	0.257	2458744.68167	49.47	1.10	0.267
2455790.77201	−29.42	1.02	0.255	2458744.68998	46.72	1.15	0.251
2455793.79756	−29.46	0.93	0.246	2459153.66133	29.66	0.79	0.222
2455796.77370	−28.75	1.03	0.246	2459153.66421	30.49	0.81	0.232
2455796.77832	−29.11	1.19	0.263	2459153.66720	30.10	0.81	0.224
2456139.75501	−23.85	1.06	0.248	2459363.89612	24.41	0.94	0.211
2456175.76174	−26.57	1.04	0.262	2459363.89946	24.76	0.92	0.223
2456176.72566	−28.48	1.03	0.234	2459447.69813	14.24	0.83	0.214
2456501.82731	−14.66	0.96	0.239	2459447.70012	15.71	0.87	0.205
2456550.66118	−18.60	0.92	0.249	2459447.70211	15.95	0.82	0.205
2456552.67848	−17.30	1.10	0.240	2459447.70413	16.88	0.81	0.212
2456604.60810	−14.66	0.79	0.241	2459507.67315	12.93	0.89	0.203
2456607.58228	−10.50	1.02	0.237	2459507.67574	11.37	0.79	0.211
2456818.94017	−8.20	0.99	0.231	2459507.67833	11.76	0.87	0.208
2456867.83024	−11.15	1.01	0.214	2459748.92057	3.25	0.97	0.227
2456871.77590	−11.73	0.87	0.220	2459748.92316	3.14	0.91	0.227
2457260.79250	0.00	0.88	0.246	2459748.92580	4.47	0.88	0.227
2457319.66988	−1.44	0.90	0.235	2459829.72691	−0.71	0.97	0.223
2457326.61668	−2.51	0.88	0.233	2459829.72941	−1.13	0.94	0.221
2457536.93357	6.80	1.09	0.244	2459829.73202	−1.42	0.95	0.225
2457555.92679	7.15	0.90	0.228	2459861.65634	0.18	0.86	0.214
2457616.77039	10.82	0.87	0.212	2459861.65892	−1.42	0.81	0.214
2457619.78799	8.38	1.11	0.342	2459861.66147	−0.91	0.94	0.227
2457737.54332	12.65	0.88	0.218	2459890.54516	−4.26	0.92	0.240
2458271.85419	44.44	0.90	0.210	2459890.55021	−3.55	0.94	0.236
2458293.88374	39.93	0.81	0.204	2460124.93080	−7.41	0.88	0.223
2458675.82705	47.65	0.89	0.220	2460124.93330	−9.37	0.92	0.218
2458675.83079	47.53	0.98	0.226	2460124.93589	−7.52	0.80	0.215
2458675.83326	47.09	0.92	0.227				

Table A2. AAT RVs for HD 222237.

BJD	RV [m s^{-1}]	Error [m s^{-1}]	BJD	RV [m s^{-1}]	Error [m s^{-1}]
2451034.23140	−4.92	1.93	2453042.91623	0.89	1.94
2451385.32779	−14.86	3.34	2453245.21460	−0.50	1.62
2451473.08162	−0.28	2.24	2453570.24266	−3.32	1.44
2451745.25030	−8.45	2.42	2453947.27765	−0.36	1.26
2451830.07472	1.99	4.38	2454041.05363	−2.61	1.49
2451920.94390	−2.50	2.50	2454255.22288	−1.10	1.50
2452128.21848	−1.44	1.76	2454371.18539	1.63	1.28
2452152.02008	−10.86	2.21	2454777.07424	−2.18	1.10
2452187.10631	−6.09	1.35	2455106.14845	1.23	1.87
2452456.27032	−5.94	1.78	2455846.00705	15.31	1.49
2452511.05088	−2.23	1.53	2456140.23712	25.33	1.83
2452591.98274	−3.04	1.06	2456465.31881	35.88	1.77
2452593.98191	−0.54	1.77	2456556.08965	29.32	1.45
2452594.99536	−4.84	1.56	2456935.12973	34.35	1.60
2452598.98813	−4.48	1.82	2456939.09431	21.83	1.87
2452787.29273	−1.46	2.78	2457236.26158	51.22	2.73
2452861.27062	−0.28	2.55	2457346.01176	44.06	2.34
2452945.08777	−1.35	1.82			

APPENDIX B: DETAILED METHODOLOGY**B1 RV model**

For an elliptical orbit, the distances of a star from the system's barycentre and the star's z -coordinate along the lines of sights are, respectively,

$$r(t) = \frac{a_*(1 - e^2)}{1 + e \cos v(t)}, \text{ and} \quad (\text{B1})$$

$$z(t) = r(t) \sin i \sin(\omega + v(t)), \quad (\text{B2})$$

where a_* is the semimajor axis of the primary star relative to the system's barycentre, e is the eccentricity, i is the inclination, ω is the argument of periastron of the stellar reflex motion, and $v(t)$ is the true anomaly and is related to the eccentric anomaly, $E(t)$, which is given by

$$\tan \frac{v(t)}{2} = \sqrt{\frac{1+e}{1-e}} \cdot \tan \frac{E(t)}{2}. \quad (\text{B3})$$

This relation can be derived geometrically. The mean anomaly $M(t)$ at a specific time is then defined as

$$M(t) = \frac{2\pi}{P}(t - T_p). \quad (\text{B4})$$

According to Kepler's equation, the relation between $M(t)$ and $E(t)$ is given by

$$M(t) = E(t) - e \sin E(t). \quad (\text{B5})$$

Thus, the variation of stellar RVs due to a companion at epoch t_j is

$$\hat{v}_j = \dot{z} = K[\cos(\omega + v(t_j)) + e \cos(\omega)], \quad (\text{B6})$$

where K is the semi-amplitude and can be written as

$$K \equiv \frac{2\pi}{P} \frac{a_* \sin i}{\sqrt{1 - e^2}}. \quad (\text{B7})$$

Therefore, the likelihood for the measured RV ($v_{j,k}$) can be calculated by

$$\mathcal{L}_{\text{RV}} = \prod_{j=1}^{N_{\text{RV}}} \prod_{k=1}^{N_{\text{inst}}} \frac{1}{\sqrt{2\pi(\sigma_{j,k}^2 + \sigma_{\text{jit},k}^2)}} \exp\left(-\frac{(v_{j,k} - \hat{v}_{j,k} - \gamma_k)^2}{2(\sigma_{j,k}^2 + \sigma_{\text{jit},k}^2)}\right), \quad (\text{B8})$$

where N_{RV} and N_{inst} are, respectively, the number of RV measurements and instruments, and γ_k and $\sigma_{\text{jit},k}$ are, respectively, the RV offset and the so-called 'RV jitter' for different instruments.

B2 Gaia astrometric model

In rectangular coordinates, the Thiele–Innes coefficients A , B , F , G are defined as

$$A = \cos \omega \cos \Omega - \sin \omega \sin \Omega \cos i, \quad (\text{B9})$$

$$B = \cos \omega \sin \Omega + \sin \omega \cos \Omega \cos i, \quad (\text{B10})$$

$$F = -\sin \omega \cos \Omega - \cos \omega \sin \Omega \cos i, \quad (\text{B11})$$

$$G = -\sin \omega \sin \Omega + \cos \omega \cos \Omega \cos i, \quad (\text{B12})$$

where Ω is the longitude of the ascending node. Besides, the elliptical rectangular coordinates X and Y are functions of the eccentric anomaly $E(t)$ and the eccentricity e , which are given by

$$X = \cos E(t) - e \quad (\text{B13})$$

$$Y = \sqrt{1 - e^2} \cdot \sin E(t). \quad (\text{B14})$$

Therefore, the projected offsets of stellar reflex motion relative to the system's barycentre are then given by

$$\Delta\alpha_*^r = a_* \varpi (BX + GY), \quad (\text{B15})$$

$$\Delta\delta^r = a_* \varpi (AX + FY), \quad (\text{B16})$$

where $\Delta\delta^r$ and $\Delta\alpha_*^r = \Delta\alpha^r \cos \delta^r$ are the offsets in declination and right ascension, respectively, and ϖ is the parallax in units of mas. It is noted that we assume the companion is fainter than its host, and therefore its luminosity contributed to the system's photocentre is negligible (photocentre is equal to barycentre). Next, we model the astrometry of TSB at the GDR3 epoch ($t_{\text{DR3}} = \text{J2016.0}$) as follows:

$$\alpha_{\text{DR3}}^b = \alpha_{\text{DR3}} - \frac{\Delta\alpha_*}{\cos \delta_{\text{DR3}}} \quad (\text{B17})$$

$$\delta_{\text{DR3}}^b = \delta_{\text{DR3}} - \Delta\delta \quad (\text{B18})$$

$$\varpi_{\text{DR3}}^b = \varpi_{\text{DR3}} - \Delta\varpi \quad (\text{B19})$$

$$\mu_{\alpha\text{DR3}}^b = \mu_{\alpha\text{DR3}} - \Delta\mu_{\alpha} \quad (\text{B20})$$

$$\mu_{\delta\text{DR3}}^b = \mu_{\delta\text{DR3}} - \Delta\mu_{\delta}, \quad (\text{B21})$$

where α , δ , μ_{α} , μ_{δ} are right ascension, declination, and corresponding proper motions, and the subscript DR3 and the superscript b represent quantities of GDR3 and TSB astrometry, respectively. Above five quantities with Δ are barycentre offsets relative to GDR3 astrometry, and will be set as free parameters. The TSB astrometry at reference epoch t_k ($k = 1, 2$ represent GDR2, GDR3) can be modelled through linear propagation in the Cartesian coordinate as follows (Lindgren et al. 2012; Feng et al. 2019a):

$$\begin{bmatrix} x \\ y \\ z \end{bmatrix} = d \begin{bmatrix} \cos \alpha^b & \cos \delta^b \\ \sin \alpha^b & \cos \delta^b \\ \sin \delta^b \end{bmatrix}, \begin{bmatrix} v_x \\ v_y \\ v_z \end{bmatrix} = \begin{bmatrix} \cos \delta^b \cos \alpha^b & -\sin \delta^b \cos \alpha^b & -\sin \alpha^b \\ \cos \delta^b \sin \alpha^b & -\sin \delta^b \sin \alpha^b & \cos \alpha^b \\ \sin \delta^b & \cos \delta^b & 0 \end{bmatrix} \begin{bmatrix} v_r \\ v_{\delta} \\ v_{\alpha} \end{bmatrix}, \begin{bmatrix} x_k \\ y_k \\ z_k \end{bmatrix} = \begin{bmatrix} x \\ y \\ z \end{bmatrix} + \Delta t_k \begin{bmatrix} v_r \\ v_{\delta} \\ v_{\alpha} \end{bmatrix}, \quad (\text{B22})$$

and

$$\begin{bmatrix} v_{rk}^b \\ \mu_{\alpha k}^b d_k \\ \mu_{\delta k}^b d_k \end{bmatrix} = \begin{bmatrix} \cos \delta_k^b & 0 & \sin \delta_k^b \\ 0 & 1 & 0 \\ -\sin \delta_k^b & 0 & \cos \delta_k^b \end{bmatrix} \begin{bmatrix} \cos \alpha_k^b & \sin \alpha_k^b & 0 \\ -\sin \alpha_k^b & \cos \alpha_k^b & 0 \\ 0 & 0 & 1 \end{bmatrix} \begin{bmatrix} v_x \\ v_y \\ v_z \end{bmatrix}, \quad (\text{B23})$$

where $d = 1/\varpi^b$, $v_{\delta} = \mu_{\delta}^b d$, $v_{\alpha} = \mu_{\alpha}^b d$, $v_r \approx \text{RV}_{\text{DR3}}$, $d_k = \sqrt{x_k^2 + y_k^2 + z_k^2} = 1/\varpi_k^b$, and Δt_k represents the difference between t_k and t_{DR3} . Once we obtain the Cartesian state vector $(x_k, y_k, z_k, v_x, v_y, v_z)$ at t_k , we can transform them back to the equatorial state vector $(\alpha_k^b, \delta_k^b, \mu_{\alpha k}^b, \mu_{\delta k}^b, \varpi_k^b, v_{rk}^b)$. Since the GDR3 RVs are not precise enough to constrain the reflex motion, we only use them to propagate astrometry of TSB. This propagation in Cartesian coordinate system instead of spherical coordinate system can effectively avoid the problem of perspective acceleration.

By combining the linear motion of TSB and the target reflex motion in the equatorial coordinate system, we can simulate the *Gaia* and *Hipparcos* AL abscissae directly. To obtain GDR3 abscissae, we first simulate the position of the target at GOST epoch t_j relative to t_{DR3} using

$$\Delta\alpha_{*j} = \Delta\alpha_{*\text{DR3}}^b + \mu_{\alpha\text{DR3}}^b(t_j - t_{\text{DR3}}) + \Delta\alpha_{*j}^r \quad (\text{B24})$$

$$\Delta\delta_j = \Delta\delta_{\text{DR3}}^b + \mu_{\delta\text{DR3}}^b(t_j - t_{\text{DR3}}) + \Delta\delta_j^r, \quad (\text{B25})$$

where $\Delta\alpha_{*\text{DR3}}^b = (\alpha_{\text{DR3}}^b - \alpha_{\text{DR3}}) \cos \delta_{\text{DR3}}^b$, and $\Delta\delta_{\text{DR3}}^b = \delta_{\text{DR3}}^b - \delta_{\text{DR3}}$. Since the reflex motion induced by substellar companions is not as significant as linear barycentric motion, we approximate the parallax at t_j as $\varpi_j \approx \varpi_{\text{DR3}}^b$. Then we project the above target position on to the 1D AL direction by considering the parallactic perturbation of *Gaia* satellite's heliocentric motion, using

$$\eta_j = \Delta\alpha_{*j} \sin \psi_j + \Delta\delta_j \cos \psi_j + \varpi_{\text{DR3}}^b f_j^{\text{AL}}, \quad (\text{B26})$$

where η_j is AL abscissa, ψ_j is the scan angle of *Gaia* satellite, and f_j^{AL} is the parallax factor from GOST. Finally, we model the simulated abscissae with a five-parameter model as follows:

$$\hat{\eta}_j = \Delta\alpha_{*\text{DR3}}^l \sin \psi_j + \Delta\delta_{\text{DR3}}^l \cos \psi_j + \hat{\varpi}_{\text{DR3}} f_j^{\text{AL}}, \quad (\text{B27})$$

$$\Delta\alpha_{*\text{DR3}}^l = (\hat{\alpha}_{\text{DR3}} - \alpha_{\text{DR3}}) \cos \hat{\delta}_{\text{DR3}} + \hat{\mu}_{\alpha\text{DR3}}(t_j - t_{\text{DR3}}), \quad (\text{B28})$$

$$\Delta\delta_{\text{DR3}}^l = (\hat{\delta}_{\text{DR3}} - \delta_{\text{DR3}}) + \hat{\mu}_{\delta\text{DR3}}(t_j - t_{\text{DR3}}). \quad (\text{B29})$$

Above modelling can give a set of model parameters $(\hat{\alpha}_{\text{DR3}}, \hat{\delta}_{\text{DR3}}, \hat{\mu}_{\alpha\text{DR3}}, \hat{\mu}_{\delta\text{DR3}}, \hat{\varpi}_{\text{DR3}})$ at t_{DR3} . Likewise, modelling GDR2 astrometry can be done easily by changing the subscript DR3 to DR2 , but keeping the reference position fixed in GDR3. Given that the *Gaia* IAD is not available, we assume each individual observation has the same uncertainty and thus will be assigned equal weighting when fitting for the five-parameter model. Besides, we take into account the published astrometric gaps (e.g. dead times and rejected observations) when modelling abscissae. To avoid numerical errors, we define the catalogue astrometry at t_k relative to t_{DR3} as follows:

$$\Delta\vec{t}_k \equiv (\Delta\alpha_{*k}, \Delta\delta_k, \Delta\varpi_k, \Delta\mu_{\alpha k}, \Delta\mu_{\delta k}) = ((\alpha_k - \alpha_{\text{DR3}}) \cos \delta_k, \delta_k - \delta_{\text{DR3}}, \varpi_k - \varpi_{\text{DR3}}, \mu_{\alpha k} - \mu_{\alpha\text{DR3}}, \mu_{\delta k} - \mu_{\delta\text{DR3}}). \quad (\text{B30})$$

Likewise, the fitted astrometry at t_k is $\hat{\Delta\vec{t}}_k$. The likelihood for GDR2 and GDR3 can be written as

$$\mathcal{L}_{\text{gaia}} = \prod_{k=1}^{N_{\text{DR}}} \frac{1}{\sqrt{(2\pi)^5 |\Sigma_k(S^2)|}} \exp \left(-\frac{1}{2} (\Delta\vec{t}_k - \hat{\Delta\vec{t}}_k)^T [\Sigma_k(S^2)]^{-1} (\Delta\vec{t}_k - \hat{\Delta\vec{t}}_k) \right), \quad (\text{B31})$$

where N_{DR} represents the number of *Gaia* data releases ($N_{\text{DR}} = 2$ if we use both GDR2 and GDR3), Σ_k is the catalogue covariance for the five parameters, and S is the error inflation factor for *Gaia* astrometry. Given that the covariance given by *Gaia* catalogue is probably underestimated, we can use the error inflation S and jitter J to construct a new covariance as $\Sigma_{mn} = \rho_{mn} \sqrt{S^2 \sigma_n^2 + J^2} \sqrt{S^2 \sigma_k^2 + J^2}$, where ρ

is the correlation matrix. As indicated by Feng et al. (2024) (see their table 1) who employs orbital solutions from the GDR3 non-single-star catalogue (Halbwachs et al. 2023; Holl et al. 2023) to estimate the error inflation within the astrometric catalogues, no significant jitter and error inflation are found existing in both GDR2 and GDR3, and this finding remains robust across different choices of calibration sources. We thus use a strong Gaussian distribution as the prior to constrain the error inflation, as well as setting jitter to zero.

B3 *Hipparcos* astrometric model

Similar to *Gaia* astrometric model, we first propagate the TSB astrometry at t_{DR3} to *Hipparcos* reference epoch t_{HIP} . Then we simulate the position of target at *Hipparcos* epoch using

$$\Delta\alpha_{*j} = \Delta\alpha_{*j}^b + \Delta\mu_{\alpha\text{HIP}}^b(t_j - t_{\text{HIP}}) + \Delta\alpha_{*j}^r, \quad (\text{B32})$$

$$\Delta\delta_j = \Delta\delta_{\text{HIP}}^b + \Delta\mu_{\delta\text{HIP}}^b(t_j - t_{\text{HIP}}) + \Delta\delta_j^r, \quad (\text{B33})$$

where $\Delta\alpha_{*j}^b = (\alpha_{\text{HIP}}^b - \alpha_{\text{HIP}}) \cos(\Delta\delta_{\text{HIP}}^b/2)$, $\Delta\delta_{\text{HIP}}^b = \delta_{\text{HIP}}^b - \delta_{\text{HIP}}$, $\Delta\mu_{\alpha\text{HIP}}^b = \mu_{\alpha\text{HIP}}^b - \mu_{\alpha\text{HIP}}$, and $\Delta\mu_{\delta\text{HIP}}^b = \mu_{\delta\text{HIP}}^b - \mu_{\delta\text{HIP}}$. Therefore, the abscissae of *Hipparcos* is given by

$$\hat{\xi}_j = \Delta\alpha_{*j} \cos \psi_j + \Delta\delta_j \sin \psi_j + \Delta\varpi_{\text{HIP}}^b f_j^{\text{AL}}, \quad (\text{B34})$$

where $\Delta\varpi_{\text{HIP}}^b = \varpi_{\text{HIP}}^b - \varpi_{\text{HIP}}$. Above three formulae are slightly different from those of *Gaia*. We additionally correct the difference between *Hipparcos* astrometry and the astrometry propagated from the GDR3 epoch to the *Hipparcos* epoch. Besides, the scan angle in the new *Hipparcos* IAD is complementary with *Gaia* scan angle. Finally, we can calculate the likelihood for *Hipparcos* IAD using

$$\mathcal{L}_{\text{hip}} = \prod_{j=1}^{N_{\text{IAD}}} \frac{1}{\sqrt{2\pi(\sigma_j^2 + J_{\text{hip}}^2)}} \exp\left(-\frac{(\hat{\xi}_j - \xi_j)^2}{2(\sigma_j^2 + J_{\text{hip}}^2)}\right), \quad (\text{B35})$$

where N_{IAD} is the total number of *Hipparcos* IAD, σ_j is the individual measurement uncertainty, and J_{hip} is the jitter term.

APPENDIX C: ADDITIONAL FIGURES

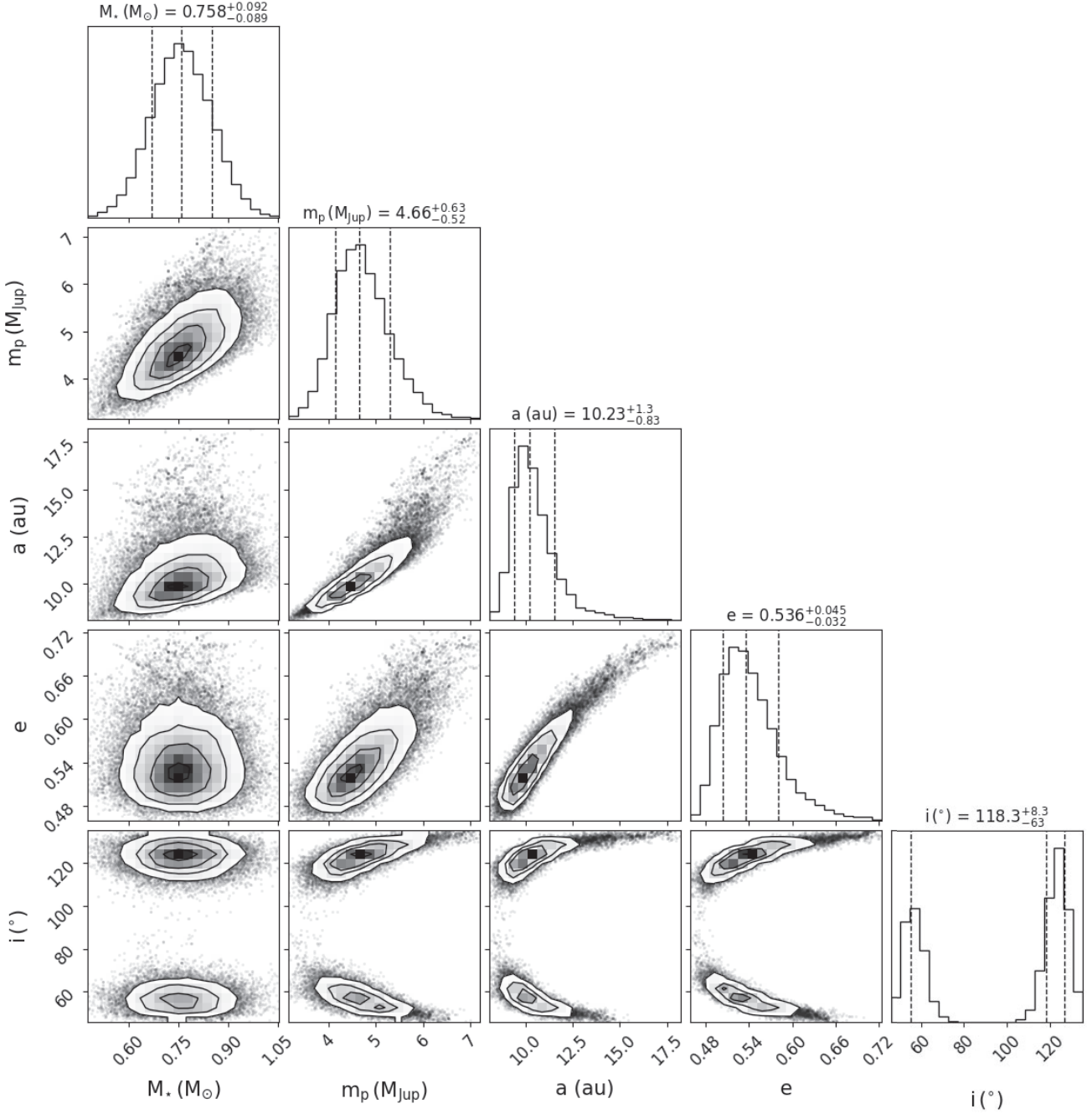


Figure C1. Posterior distributions for selected orbital parameters by *orvara* (RV+HGCA). The median and the corresponding 1σ confidence intervals are denoted by vertical dashed lines.

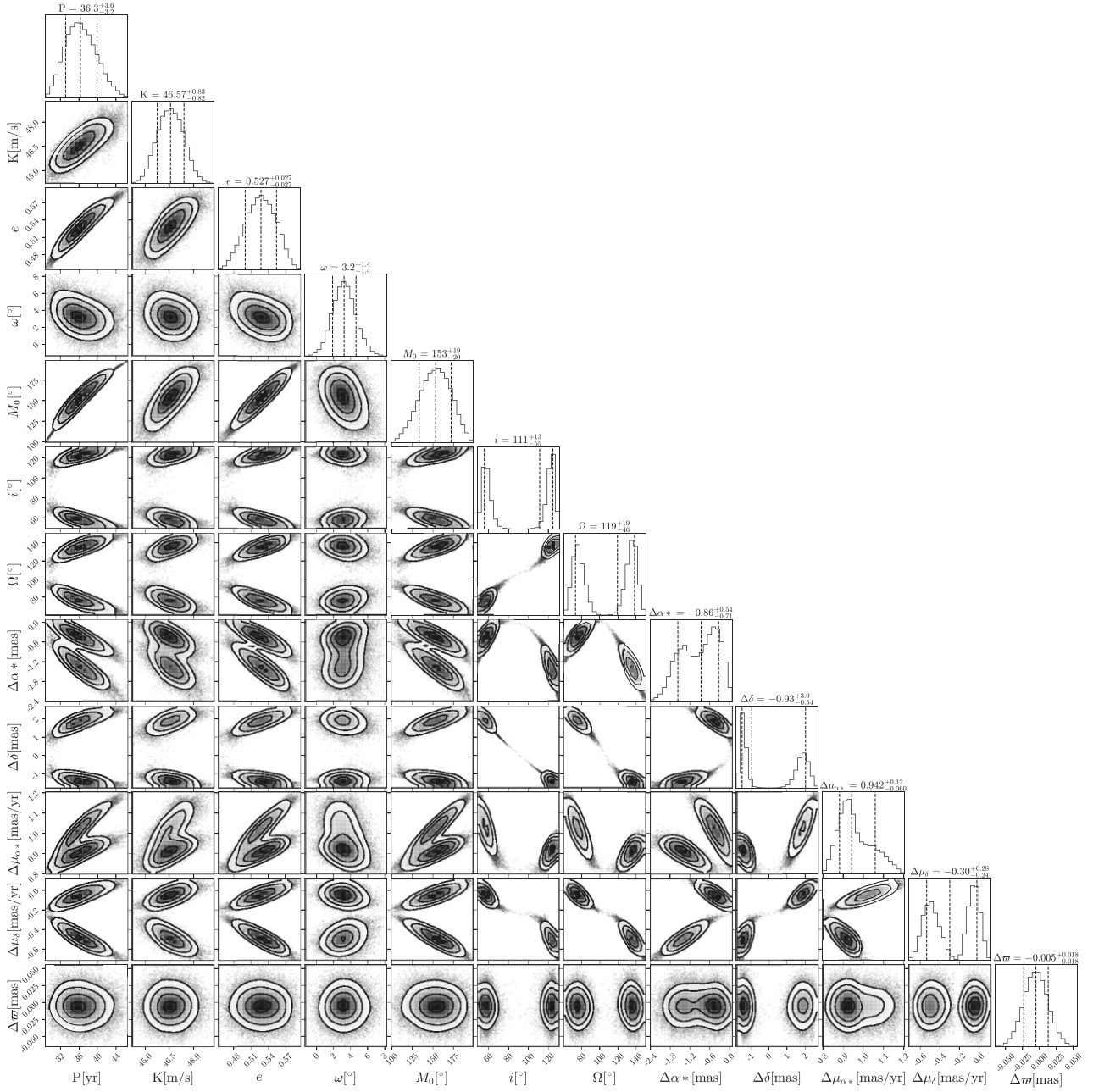


Figure C2. Posterior distributions for selected orbital parameters by RV+HG3. The bimodal distributions of i , Ω , $\Delta\alpha^*$, $\Delta\delta$, $\Delta\mu_{\alpha^*}$, and $\Delta\mu_{\delta}$ can be recognized.

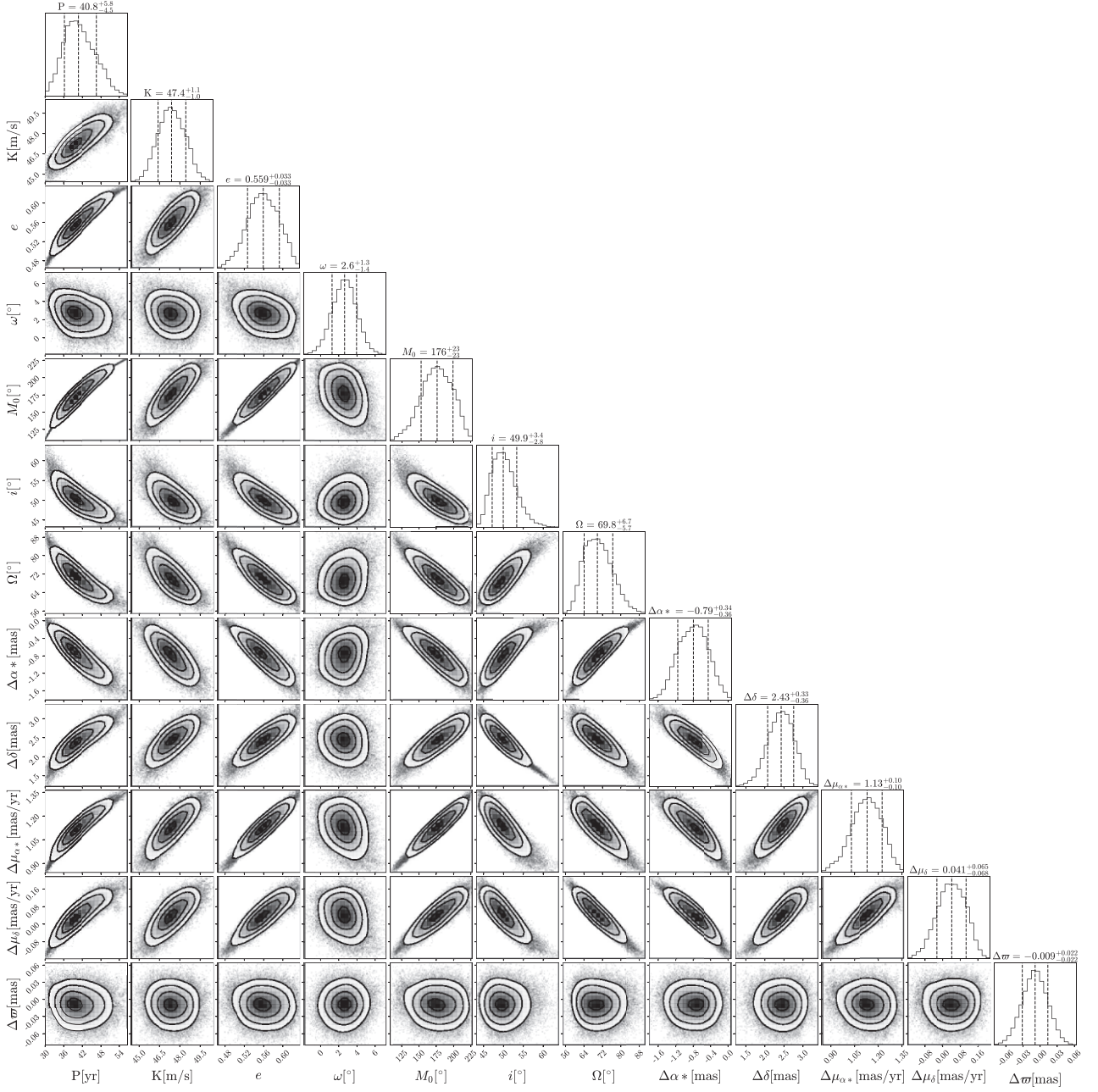


Figure C3. Posterior distributions for selected orbital parameters by RV+HG23. With the inclusion of GDR2, the ambiguities for i , Ω , $\Delta\alpha^*$, $\Delta\delta$, $\Delta\mu_{\alpha^*}$, and $\Delta\mu_\delta$ are well resolved.

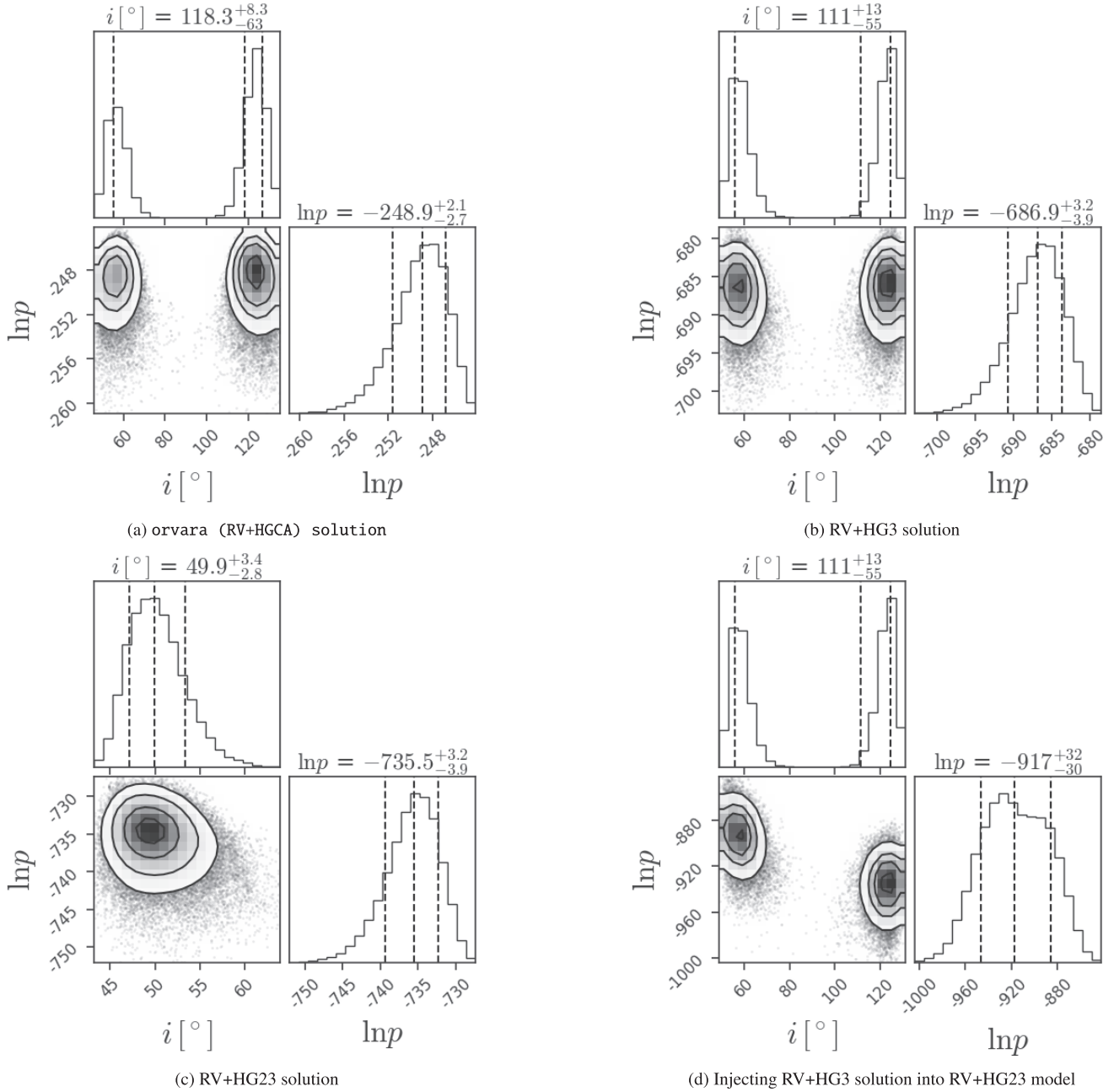


Figure C4. Comparing the inclination posterior distribution of different solutions. The inclination obtained from *orvara* (a) and RV+HG3 (b) exhibits bimodal distribution, and the two modes have equivalent posterior probability, while RV+HG23 (c) has the ability to break the inclination degeneracy. When RV+HG3 solution is injected into RV+HG23 model (d), we found that the higher inclination (corresponding to the retrograde orbital solution) can be rejected, suggesting the precision of *Gaia*, along with the baseline between GDR2 and GDR3, is sufficient to obtain an unambiguous orbital orientation of HD 222237 b.

This paper has been typeset from a \LaTeX file prepared by the author.